Linford Matthew R. (Orcid ID: 0000-0003-0460-041X)
Morgan David (Orcid ID: 0000-0002-6571-5731)
Baltrusaitis Jonas (Orcid ID: 0000-0001-5634-955X)

Definition of a New (Doniach-Sunjic-Shirley) Peak Shape for Fitting Asymmetric Signals Applied to Reduced Graphene Oxide/Graphene Oxide XPS Spectra

Behnam Moeini,[1] Matthew R. Linford,[1] Neal Fairley,[2] Anders Barlow,[3] Peter Cumpson[4] David Morgan,[5,6] Vincent Fernandez,[7] and Jonas Baltrusaitis[8,]*

[1]Department of Chemistry and Biochemistry, Brigham Young University, Provo, UT, 84602 USA
[2]Casa Software Ltd, Bay House, 5 Grosvenor Terrace, Teignmouth, Devon TQ14 8NE, UK
[3]Materials Characterisation and Fabrication Platform, Department of Chemical Engineering, University of Melbourne, Melbourne, Victoria 3010, Australia
[4]Mark Wainwright Analytical Centre, University of New South Wales, Sydney, New South Wales, Australia
[5]School of Chemistry, Cardiff University, Main Building, Park Place, Cardiff CF10 3AT, United Kingdom
[6]HarwellXPS – EPSRC National Facility for Photoelectron Spectroscopy, Research Complex at Harwell (RCaH), Didcot, Oxon, OX11 0FA
[7]Institut des Matériaux Jean Rouxel (IMN), Université de Nantes, CNRS, 2 rue de la Houssinière, BP 32229, 44322 Nantes cedex 3, France
[8]Department of Chemical and Biomolecular Engineering, Lehigh University, 111 Research Drive, Bethlehem, PA 18015, USA

Abstract

The existence of asymmetry in X-ray Photoelectron Spectroscopy (XPS) photoemission lines is widely accepted, but line shapes designed to accommodate asymmetry are generally lacking in theoretical justification. In this work, we present a new line shape for describing asymmetry in XPS signals that is based on two facts. First, the most widely known line shape for fitting asymmetric XPS signals that has a theoretical basis, referred to as the Doniach-Sunjic (DS) line shape, suffers from a mathematical inconvenience, which is that for asymmetric shapes the area beneath the curve (above the x-axis) is infinite. Second, it is common practice in XPS to remove the inelastically scattered background response of a peak in question with the Shirley algorithm. The new line shape described herein attempts to retain the theoretical virtues of the DS line shape, while allowing the use of a Shirley background, with the consequence that the resulting line shape has a finite area. To illustrate the use of this Doniach-Sunjic-Shirley (DSS) line shape, a set of spectra obtained from varying amounts of graphene oxide (GO) and reduced GO on a patterned, heterogeneous surface are fit and discussed.

*Corresponding author: job314@lehigh.edu; +1-610-758 6836

Keywords: XPS; peak shape; data processing; reduced; graphene oxide

Introduction

Peak shapes used to fit X-ray photoelectron spectroscopy (XPS) data represent a constraint on optimization that can force more physically meaningful outcomes. Hence, XPS peak fitting is best performed using peak models (functional forms) designed with the best possible shapes for each component. Several different peak shapes have been designed and used for XPS peak fitting [1–3], which become increasingly important as material complexity increases. For example, complex oxides are employed/developed in heterogeneous catalysis, the semiconductor industry, and in thin film deposition [4,5,14–20,6–13]. Application of XPS to these surfaces often results in complex spectral envelopes produced by multiple chemical states that may manifest themselves as asymmetric signals. Here, the asymmetric component(s) at (typically) lower binding energies influence the higher binding energy peaks within a given peak model. When estimating the ratios of these types of chemical states in peak fitting, it is advantageous to have line shapes that can accurately describe such asymmetry. It has recently been shown that a significant fraction of the XPS data in the scientific literature has been fit improperly [21–23]. Accordingly, a better understanding of XPS, including the development of new functional forms (peak shapes) is an important and current topic. Recent efforts have been made to provide the community with guides on the acquisition and analysis of XPS data, including peak fitting [22,24–26].

Since its introduction, the Doniach-Sunjic (DS) line shape has been called into question because its asymmetric, closed-form mathematical description integrates to infinity [27]. Accordingly, while the DS line shape may provide a tool for fitting asymmetric XPS data, the meaning one assigns to it is entirely arbitrary. Nevertheless, there are photoemission peaks for which asymmetric line shapes are important, but selecting line shapes from the various *ad hoc* functions designed to allow for asymmetry based on data alone is problematic because data rarely provide enough guidance to identify the true line shape for a given photoemission peak. An approach based on physics is always preferable to *ad hoc* methods. Indeed the Doniach-Sunjic method follows a logic based on physics, and there is a need to create a line shape that follows its shape for asymmetry, but with the additional essential property of a finite area.

The mathematics of photoemission and background curves are fundamentally different. While the quantized nature of energy levels for electrons bound to atoms suggests photoemission without energy loss should be countable and proportional to the number of atoms from which photoemission occurs, the same link between the number of atoms and the background signal is not expected for XPS data. That is, the background signal originates from atoms that may not be involved in generating a zero-loss signal. Furthermore, the background signal in XPS is not limited to a single photoemission process but results from all photoemission processes that generate electrons with initial kinetic energies greater than that of a specific photoelectron peak or region. Thus, one does not expect a background curve to mathematically integrate to a finite area for infinite limits. For example, the Shirley algorithm [28] commonly used to remove the inelastically scattered background asymptotically approaches a non-zero value as energy approaches negative infinity, i.e., extended to plus and minus infinity, the integral of a Shirley background is infinite [29].

The use and results of any line shape always depends on the method used to remove the background signal. This statement is a simple consequence of the fact that a synthetic envelope is formed by summing the background along with all the synthetic fit components in proportions necessary to fit the data envelope. That is, even when a background curve is computed directly from the data, its shape contributes to the final synthetic envelope. Accordingly, if the background intensity increases, the photoemission intensity must decrease, and *vice versa*, i.e., changes to the shape of one must necessarily affect the shape of the other. While classifying the curves used in peak models as either photoemission or background is useful, we note that the DS curve fits into neither classification precisely. Therefore, it can be asked: in what sense does the DS profile represent the photoemission signal? Since the area of asymmetric DS line shapes is infinite, one answer is that the DS line shape has characteristics of both a photoemission peak and also of a curve that represents energy loss similar to a background. Thus, if it is assumed that the infinite area for the DS profile is due to its background characteristics, one method to modify it would be to subtract a curve with the shape expected for energy loss events during photoemission. If one limits the use of the DS line shape to materials with small band gaps, then the Shirley algorithm can be justified as the form for a background curve that can be removed from the DS line shape.

Following the logic described above, we define a new line shape that we refer to as the Doniach-Sunjic-Shirley (DSS) line shape. It is based on the original DS profile with an added energy loss curve modeled by the Shirley algorithm. Here, the DS line shape parameters are augmented by a third parameter that controls the energy offset between the DS profile maximum and the point along the DS profile curve at which a Shirley shape computed from the DS profile becomes equal to the DS profile. After mathematically defining this new peak shape, we present an example of a repeated, automated analysis with a peak model in which asymmetry plays a significant role. Here, C 1s spectral image data collected from a patterned sample composed of graphene oxide (GO) and reduced GO provides a challenging application for non-linear optimization, which is made possible by the use of the asymmetric DSS line shape devised in this work.

Methods

Shirley Background Profile

For any synthetic line shape $F(x)$ a Shirley background, SB, is computed as follows.

$$SB[F(x)] = \int_x^{\infty} F(\varphi)d\varphi \qquad (1).$$

Voigt Based Lineshapes

$$Lorentzian\colon l(x) = \frac{1}{1+4x^2} \qquad (2),$$

$$Gaussian\colon g(x\colon w) = e^{-4ln2\left(\frac{x}{w}\right)^2} \qquad (3),$$

$$LA\ Lineshape\colon LA(x\colon w) = N\int_{-\infty}^{\infty} l(\tau)g(x-\tau\colon w)d\tau \qquad (4),$$

(4),

$LA(1,n)$ is notation used to define a true Voigt line shape defined by Equation (4) where the first parameter, 1, indicates a Lorentzian, Equation (2), and $w = w(n)$. The parameter n in $LA(1,n)$ specifies the width w for a Gaussian that is convolved with the Lorentzian (Equation (4)) to obtain a Voigt line shape.

Mathematical definition of the new Doniach-Sunjic-Shirley (DSS) Line Shape

The Doniach-Sunjic profile P with asymmetry parameter α is defined by (5)

$$P(x,\alpha) = \frac{1}{[1+4x^2]^{\frac{1-\alpha}{2}}} \times cos\left(\frac{\pi\alpha}{2} + (1-\alpha)tan^{-1}(2x)\right) \qquad (5).$$

A line shape is derived from the Doniach-Sunjic profile by convolution with a Gaussian, g, in Equation (3), of width characterized by the parameter n according to (6)

$$DS(x,\alpha,n) = P(x,\alpha) * g(x\colon w(n)) \qquad (6).$$

We note that for $\alpha = 0$, $cos\left(\frac{\pi\alpha}{2} + (1-\alpha)tan^{-1}(2x)\right) = \frac{1}{[1+4x^2]^{\frac{1}{2}}}$ and therefore $P(x,0)$ is a Lorentzian, hence $DS(x,0,n) = P(x,0) * g(x\colon w(n))$ is a Voigt line shape. We describe the lineshape in the figures herein as DS(α,n) where the value of α is the first adjustable parameter in Equation (6) and n is the second adjustable parameter.

A Shirley background response for a Doniach-Sunjic profile is defined as (7)

$$SB[P(x,\alpha)] = \int_x^{\infty} P(x,\alpha)d\varphi \qquad (7).$$

The definition for a Doniach-Sunjic-Shirley profile is then as follows in Equations (8) and (9) where

$$Q(x,\alpha,n,l) = \begin{cases} 0, & x < -l \\ [P(x,\alpha) - k \times SB[P(x,\alpha)]], & x \geq -l \end{cases} \quad (8),$$

$$DSS(x,\alpha,n,l) = Q(x,\alpha,n,l) * g(x\colon w(n)) \quad (9),$$

where k is determined such that

$$SB[P(-x_l,\alpha)] = P(-x_l,\alpha) \quad (10).$$

The relationship in Equation (10) is illustrated for $l = 52$ in Figure 1(c). We describe the DSS lineshape herein as DS(α,n,l), where the value of α is the first adjustable parameter in Equation (9), n is the second adjustable parameter, and l is the third adjustable parameter.

A comparison of the DS and DSS line shapes is shown in Figure 1. The DSS line shape is constructed in terms of the DS line shape, and therefore the DSS line shape definition involves adding a third adjustable parameter to the DS line shape. The influence of the third parameter in the definition of the DS line shape is illustrated in Figure 1(b) using $\alpha = 0.1$, where three examples of the third parameter for the DSS line shapes with $\alpha = 0.1$ are compared to the DS line shape with the same value for α. Increasing the value for l in Equation 9 reduces the influence of the Shirley response to a DS line shape, and, as a result, increases the DS contribution to the asymmetric curvature in the DSS line shape.

The DSS line shape has been implemented in CasaXPS [30] starting with release 2.3.24. In CasaXPS, the DS and DSS lineshapes are polymorphic, i.e., determined by the number of parameters specified. This notation is also followed herein.

Results

Application of the Doniach-Sunjic-Shirley (DSS) Line Shape

An important example of a narrow scan that requires an asymmetric line shape is the C 1s spectrum of GO. Indeed, the specific example used in this work to demonstrate the DS-Shirley line shape is an image of GO reduced [31] in a pattern corresponding to the logo of the University of Newcastle in the UK shown in Figure 2. A detailed description of the corresponding sample preparation and instrumentation is given by Barlow et al. [31]. The datasets used to create Figures 2 and 3 of this manuscript are available as Supporting Information. XPS image data were acquired using a Thermo K-Alpha XPS instrument operating at a pass energy of 20 eV using an analysis area of 100 μm. The sample stage was moved beneath the X-ray spot in a raster pattern resulting in an image with 29 rows of 25 pixels, where each pixel represents a location on the sample at which C 1s spectra were acquired. The resulting spectra show varying proportions of GO and reduced GO. These types of spectra can sometimes be modeled using a single peak model (as demonstrated in this paper), i.e., a model with identical components with common parameter constraints, some of which are varied. Figure 3 shows representative spectra from this image that correspond to a mixture of GO and reduced GO (Figure 3a), fully reduced GO (Figure 3b), and GO (Figure 3c). The same peak model, which employs an asymmetric DSS line shape for GO, was applied to all these spectra, and also to all the spectra (pixels) that form the image shown in Figure 2. An image was then created for each component (peak) in the model. For example, Figure 2 shows the images that represent the C-C signal from reduced-GO and the C-O signal that is expected to correlate with GO intensity. The opposite contrasts of these maps are consistent with the expected chemistry of the sample.

The mode used to acquire these data was selected to provide both spatial and chemical state information. Chemical state determination requires reasonably high-resolution data. While the fitting statistics shown in Figure 3 appear consistent with pulse-counted data, the signal-to-noise in these data is lacking. In general, when mapping a sample with spatial features of a given size, the analysis area is a compromise between spatial resolution and signal-to-noise. The choice of analysis size is also affected by the fact that the sample responds differently to charge compensation at different positions on the sample. A small analysis area mitigates charge compensation issues but has other consequences. Selecting a 100 μm analysis area enhances the consistency of the data acquired at the expense of the count rate. Inconsistency in the data may occur not only as a result of charge compensation but may also vary over an analysis area due to the lens column performance off-axis, both of which alter peak shapes. The use of a 100 μm analysis area limits both of these factors. The use of a 20 eV pass energy, which also limits count rate, reduces the influence of instrumental artifacts in these data. An advantage of the 100 μm analysis area and 20 eV pass energy are that they allow spatial variations to be assessed and the construction of the two chemical state maps shown in Figure 2. In addition, the size of the analysis area affects the composition of the final spectra, particularly for heterogeneous samples. For example, a spectrum containing mixed chemical states would be expected from an analysis of the boundary between distinct zones containing GO and reduced GO. Another possibility is that partially reduced GO would be present on the surface, which would similarly give mixed chemical state data. A combination of these factors likely accounts for the spectra with mixed compositions in our data set.

The goals of peak fitting the spectra in Figure 3 are (i) to obtain a residual standard deviation (STD) close to unity (which is expected for pulse counted data), and (ii) the normalized residual should appear uniform over the energy interval involved during optimization. Both of these goals are reasonably well met. However, confidence in these objectives should be tempered when there is a lack of signal, which would permit imperfect line shapes to fit the data with good statistics. For example, photoemission measured below the detection limit can be fit using a linear curve satisfying the conditions for good data reproduction, but clearly, a bell-shaped photoemission peak is not well represented by a linear polynomial. Unfortunately, accumulating signal to improve signal-to-noise may damage a sample through extended acquisition times and potentially introduce systematic errors that prevent good fitting statistics, even for a correctly constructed peak model fit to data with good signal-to-noise. Accordingly, the experimental conditions employed to acquire the data in Figure 3 appear to have been a good compromise between the signal-to-noise of the spectra and any sample damage. Confidence in a proposed peak model is enhanced by observing that all of the spectra in a data set can be fit in a way that satisfy both of the goals listed above.

The need for an asymmetric line shape to fit the data from our patterned GO/reduced GO sample is underscored by the spectrum in Figure 3b, which shows the type of asymmetric tail characteristic of graphitic materials. This asymmetric component is also important for fitting the low binding energy feature in the spectrum in Figure 3a, which includes a signal characteristic of both reduced-GO and GO. If a single symmetric component were assumed to be appropriate for the signal responsible for the peak situated close to 285 eV, the binding energy for C-C photoemission would be poorly defined. Since the C-C peak position is often used as a reference for carbon in other oxidation states [32], its binding energy must be known as precisely as possible.

The assignment of the peaks used to fit the spectral envelopes in Figure 3, with accompanying fitting parameters, is presented in Table 1. This model is based on a recently published approach [33]. Binding energy assignments for synthetic peaks in graphitic materials may be complicated by shake-up intensity from π states with sp^2 character. As appears to be the case in Figure 3, these shake-up satellites may overlap with the signal from carbon bonded multiple times to oxygen that is chemically shifted relative to the C-C type signal. The peak model in Figure 3 includes a component assigned to a graphitic shake-up event that is labeled C 1s C-C Sat. There are also two components labeled C=O, which simply indicate here the potential for multiple bonds between carbon and oxygen. The origin of this 'C=O' signal in Figure 3 is not specified because in XPS these features could be either energy loss structures or some mixture of chemical state information and energy loss features. However, in general, the C=O signal from carbon bonded twice to oxygen appears +1.2 – 1.5 eV above the C-O signal of carbon bonded once to oxygen, and the C(O)O (carboxyl) signal from carbon bonded three times to oxygen appears +1.2 – 1.5 eV above the C=O signal from carbon bonded twice to oxygen [32].

Table 1: Line shapes and parameter constraints applied for the peak model used in Figure 3 (and throughout this work). Interval and relational constraints as implemented in CasaXPS [30] are used to enforce relationships between these parameters. The asymmetric DSS line shape is implemented as DS(0.1,200,52). Symmetric line shapes are implemented using Voigt functions defined as a special case of the generalized Voigt line shape LA(1,n) as defined in CasaXPS.

Name	Line Shape	Position constrain	FWHM constrain	Area constrain	Synthetic component label
C1s C-C	DS(0.1,200,52)	294.2 , 280.8	0.73 , 0.73	0.0 , 140977.4	A
C1s C-C Sat	LA(1,643)	A + 6.37	A * 2.679	0.0 , 55410.6	B
C1s C-O	LA(1,643)	289.6 , 285.8	0.86 , 1.19	0.0 , 153182.6	C
C1s C=O	LA(1,643)	C + 1.56	C * 1	0.0 , 153182.6	D
C1s sp^3	LA(1,343)	A + 0.4	C * 1	C * 0.873	E
C1s C=O	LA(1,643)	C + 2.60	C * 1	0.0 , 153182.6	G

If the initial parameter values in the model in Figure 3 are used without some constraints, the resulting fit lacks physical meaning. Accordingly, interval constraints are employed to limit the range of acceptable values for a given parameter, and relational constraints, which define known relationships between parameters in different components to a peak model, are used to enforce the acceptable relationship between parameters that define different components. Relational constraints link peak binding energies through a fixed offset, while the FWHM and area for components are linked through a multiplicative factor. The role played by both types of constraints is to prevent the optimization from arriving at a mathematical fit with inappropriate chemical and physical meaning. The parameter constraints used for the peak model in Figure 3 are listed in Table 1. The column labeled 'Synthetic component label' in Table 1 assigns a single letter to each component. These letters are then used to define relational constraints in the software. The following describes the uses of these constraints in the context of the peak model employed in Figure 3.

An important interval constraint in the peak model used in Figure 3 is applied to the component labeled C 1s C-C for FWHM. In this case, the interval has identical limits [0.73, 0.73] (Table 1), and therefore the FWHM for the C 1s C-C component is fixed at 0.73 eV. The motivation for fixing the FWHM for the C 1s C-C component is its asymmetry. If the FWHM is allowed to adjust during optimization, the influence of the asymmetric tail on the other components will be significant. Secondly, there is little physical meaning associated with allowing the FWHM of this asymmetric component to deviate from the value obtained for it when it is obtained from data with low oxygen content, such as the spectrum in Figure 3b. This second point is worth emphasizing since this statement supports the use of a carbon component with an FWHM that is noticeably less than the FWHM for other components fitted to this data. The FWHM for these other symmetric components is greater than 1.15 eV, where relational constraints (C*1) force all the components, except the C 1s C-C peak and its accompanying satellite peak, to have identical FWHM values. The common FWHM for these components is guided by an interval constraint applied to the component labeled C in Table 1. It would be concerning if, after optimization, the FWHM for these symmetric components was 0.73 eV, since 0.73 eV is too narrow for these types of components. However, narrow components are possible for graphitic carbon, and the data set includes examples of spectra from points on the sample with very low oxygen. Thus, fitting the peak model to the data in Figure 3b supports the assertion that the FWHM for C 1s C-C is different from the other components in the peak model, and that 0.73 eV is the most appropriate FWHM for the C 1s C-C component applied to these data.

As shown through a Monte Carlo [34] simulation in Figure 4, the relational constraints that most strongly affect stability, are (a) the link position (binding energy) between the C-C signal modeled via the Doniach-Sunjic-Shirley line shape and the C-C signal labeled C 1s sp^3, and (b) a forced link between the area for the C 1s sp^3 peak and the component representing C 1s C-O intensity. Both of these constraints are introduced through trial and error while attempting to fit the peak model to 725 spectra corresponding to 725-pixel locations on the sample/map in Figure 2. The area constraint C * 0.873 for the C 1s sp^3 peak relative to C 1s C-O is specifically determined based on spectral characteristics of GO only. While necessary for the successful application of the peak model to form the images in Figure 2, there remains a measure of uncertainty in these relational constraints owing to uncertainty in the true form for GO. That is, it is not clear that any spectra within the data set represent pure GO. This is not to say that pure GO is without representation in the sample, but spectra may not be representative of pure GO for the following reason. The components in GO, as measured by the same make of instrument, as shown below, evolve/change with beam exposure time. These changes to GO samples are not so rapid as to prevent chemical state determination of GO by XPS, but the ratio (C * 0.873) for the C 1s C-O and C1s sp^3 components is to some extent measurement dependent. Furthermore, the precise energy offset between the symmetric peak representing the C1s sp^3 signal and the asymmetric C 1s component representing reduced GO is not easily confirmed as the most appropriate for the materials measured here. However, evidence supplied in the paper by Barlow et al. [31] is consistent with the results in Figure 3, therefore the peak model in Figure 3 is thought to provide a means for estimating sp^2/sp^3 changes in modified GO.

The successful application of a peak model to data is dependent on the quality of the data in terms of its shape/features. While good signal-to-noise can be an advantage, achieving this at the expense of deformations in the peak shapes negates any advantage gained. Application of the peak model in Table 1 to the spectra from the map in Figure 2 (see Figure 5) does not return the type of low residual STD or quality of residual plot achieved for the individual spectra in Figure 3. This result is not unexpected. The analysis area is heterogeneous, and shifts in energy for spectra measured at different locations and times are observed. Therefore, given the nature of these data, the performance of the peak model fit in Figure 5 is reasonably good. However, it demonstrates the need in these types of studies for data without acquisition artifacts. Optimization relies entirely on minimizing a figure-of-merit, and the values obtained for the residual STD deviate significantly from unity. Therefore, in the absence of constraints, one should expect data of the form in Figure 5 to converge to solutions with limited physical merit.

A final point to consider about the peak model derived in this work is the background approximation. A Shirley background was used in Figure 3. The true background to GO/reduced-GO is probably more complex than can be modeled using a Shirley background calculated directly from data. However, for reduced GO, a Shirley background is justifiable, while little if any background rise is expected from sp^3-type carbon in GO. Therefore, the background of the peak model in Figure 3 is a compromise that reflects the rise in the baseline that would come from the reduced GO portion of it. Accordingly, introducing a Shirley background is acceptable, and it also highlights a deficiency in the traditional DS line shape. Namely, making use of a Shirley background for these data, and applying the common practice of forcing the background to approach data at the limits of an energy interval over which a peak model is fitted to data, is precisely why a DS line shape without modification cannot be used to obtain acceptable data reproduction when combined with a Shirley background. That is, selecting the Shirley approach to model the background signal for use with the DS line shape introduces the need to modify the DS line shape as performed in Equation 9. It is, therefore, accepted that the modification in Equation 9 is somewhat limited in physical justification, but this modification allows the essential shapes of a DS profile to be included in an analysis of the data in Figure 3.

GO degradation study

A further application of the peak model constructed for the data in Figure 3 is studying changes in GO/reduced-GO samples that occur as a consequence of measurement by XPS, i.e., sample damage. A set of experiments performed to monitor changes in GO during repeated data acquisition cycles show evidence for reduction in GO samples. These degradation studies were performed on an instrument that was similar to the one used to acquire the data in Figures 2 and 3 (Thermo K-Alpha$^+$, Cardiff University). The quantification was performed using the relative intensities of the C 1s and O 1s components, which were converted to atomic concentrations using Scofield cross-sections [35], effective attenuation lengths [36], and the Thermo K-Alpha$^+$ transmission correction.

Evolution in the chemical state of the material is illustrated through the application of the peak model that was initially constructed for pass energy 20 spectra, e.g., the data in Figure 1, to data collected with pass energy 40 and an analysis area size of 200 µm. Increasing the pass energy and measuring signal from a larger analysis area (200 µm rather than 100 µm) improves signal-to-noise statistics in spectra at the expense of energy resolution. Thus, application of the peak model with the constraints shown in Table 1 requires the relaxing of FWHM constraints to allow broader peak shapes to arise due to the lower energy resolution of the instrumental mode. A representative fit to the pass energy 40 spectra is shown in Figure 6a.

A set of 51 experiment cycles in which the C 1s and O 1s spectra were measured repeatedly shows changes to the sample composition from an initially mixed GO/reduced-GO state. These changes are quantified by use of the peak model in Table 1 with relaxed FWHM constraints, where the results of this analysis are plotted in Figures 6b and 6c. The spectra presented in this work are a subset of the spectra measured from GO. Trends in binding energy (Figure 6b) and relative intensity (Figure 6c) demonstrate that the sample does respond to measurement by XPS – the sample chemistry changes. Systematic changes in intensity can be attributed to carbon/oxygen chemistry, but the evidence from Figure 6b suggests that increasing the proportion of graphitic-like carbon also changes the apparent binding energies for signals attributed to C-O bonds, which requires some explanation. The energy offset between the C 1s C-C and C 1s C-O components decreases as the proportion of C 1s C-C increases, which could be the result of changes in the relationships between carbon bonds as the sp^2-type environment increases. Changes in carbon chemistry may also be a consequence of a sample acquiring carbon by deposition from the analysis chamber. Other data sets acquired but not shown in this work indicate that moving to a new point on the sample returns the spectral shapes to those expected for GO, therefore the observed changes to the spectra with time are unlikely to be due to significant deposition of carbon during the analysis period. Alternatively, these changes could reflect changing charge compensation responses to evolution in the chemistry of the sample at different locations on or in the sample. It is clear from all measurements performed on GO for this paper that a constant steady-state potential for the sample is difficult to maintain over an analysis area with varying proportions of GO/reduced-GO, therefore changes in apparent binding energy could be related to charge compensation. Noteworthy evidence for changes in charge compensation on the sample is the systematic evolution of both the C 1s C-O and O 1s binding energies (Figure 6b). Evidence for changes in chemistry includes the decrease in oxygen with time, coupled with decreases in the C 1s C-O intensity. It should be noted that if graphitic-like carbon forms as a layer predominantly at the sample interface to the vacuum, then attenuation of O 1s signal from buried atoms (due to increased escape depth) may result in an apparent drop in O 1s intensity (if computed using bulk relative sensitivity factors). A further point related to quantification is the impact of an asymmetric line shape for C 1s C-C on C 1s C-O component intensity. Without the use of an asymmetric line shape for C 1s C-C, the intensity for the C 1s C-O component would be higher than if an asymmetric line shape is included in the peak model. A similar comment could be made concerning the choice of background for the peak model. Therefore, trends seen in Figure 6 are influenced by the choices made when modeling the GO/reduced-GO signals.

Conclusions

Curve fitting of data from a heterogeneous (patterned) sample has been demonstrated, where the data are rich in chemical state variation. Correlation of the chemical states obtained via a peak model with spatially resolved information is facilitated by the informed use of line shapes in a peak model. Indeed, we have demonstrated how a modification (Equation 9) to the Doniach-Sunjic profile (Equation 6) allows the essential shape for the profile to be applied in conjunction with background removal by the popular Shirley approach. The approach to analyzing GO illustrated in this paper provides insights into the possible chemistry of graphene materials and further offers the possibility of identifying the sp^2/sp^3 composition of modified GO via C 1s spectra.

Acknowledgments

This work was supported as part of the Center for Understanding and Control of Acid Gas-Induced Evolution of Materials for Energy (UNCAGE-ME), an Energy Frontier Research Center funded by the U.S. Department of Energy, Office of Science, Basic Energy Sciences under Award No. DE-SC0012577.

Figures

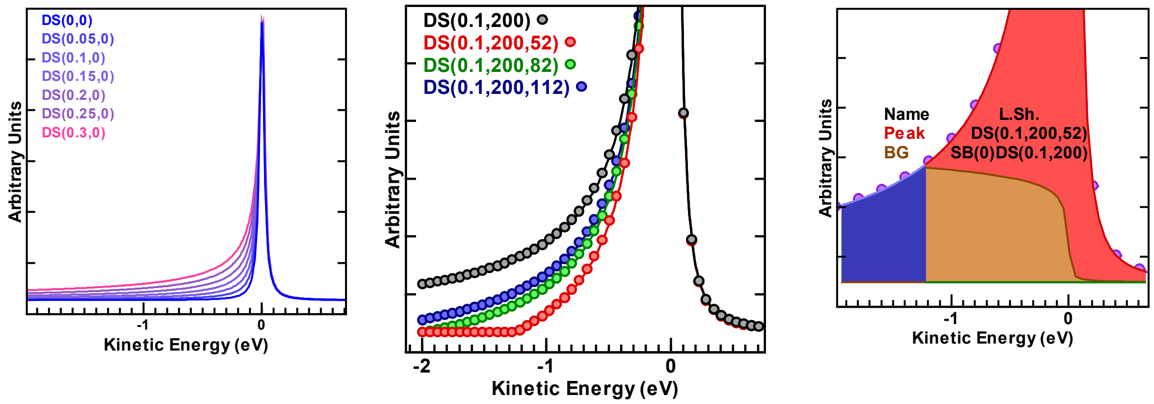

(a) (b) (c)

Figure 1. (a) A series of DS line shapes corresponding to DS(0,0) (a pure Lorentzian) to DS(0.3,0) (a pure Doniach Sunjic with substantial asymmetry). Line shapes are displayed normalized to their maximum intensity values. (b) DSS line shapes with different values of l, which is defined in Equation 9. Line shapes are displayed normalized to their maximum intensity values. (c) DS(0.1,200) line shape (purple dots) with Shirley response beneath. When the Shirley response (brown area) is subtracted from the DS(0.1,200) line shape, the DS(0.1,200,52) line shape is created, which corresponds to the red area in Figure 1a and the peak shape defined by the red dots in Figure 1b. This process excludes the blue area from the DS(0.1,200,52) line shape. The point at which the Shirley background touches the DS(0.1,200) line shape corresponds to the parameter *l* in Equation (8).

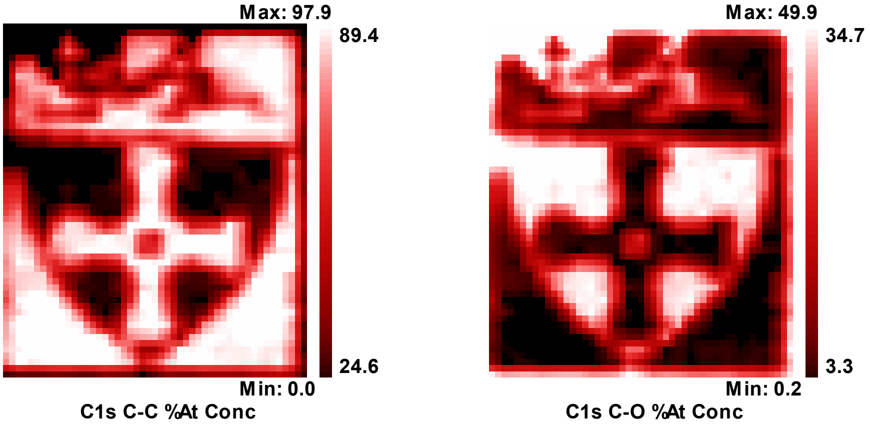

Figure 2. Chemical maps of a GO/reduced-GO sample corresponding to the C-C (left) and C-O (right) components of the peak model defined in Table 1 and used in Figure 3.

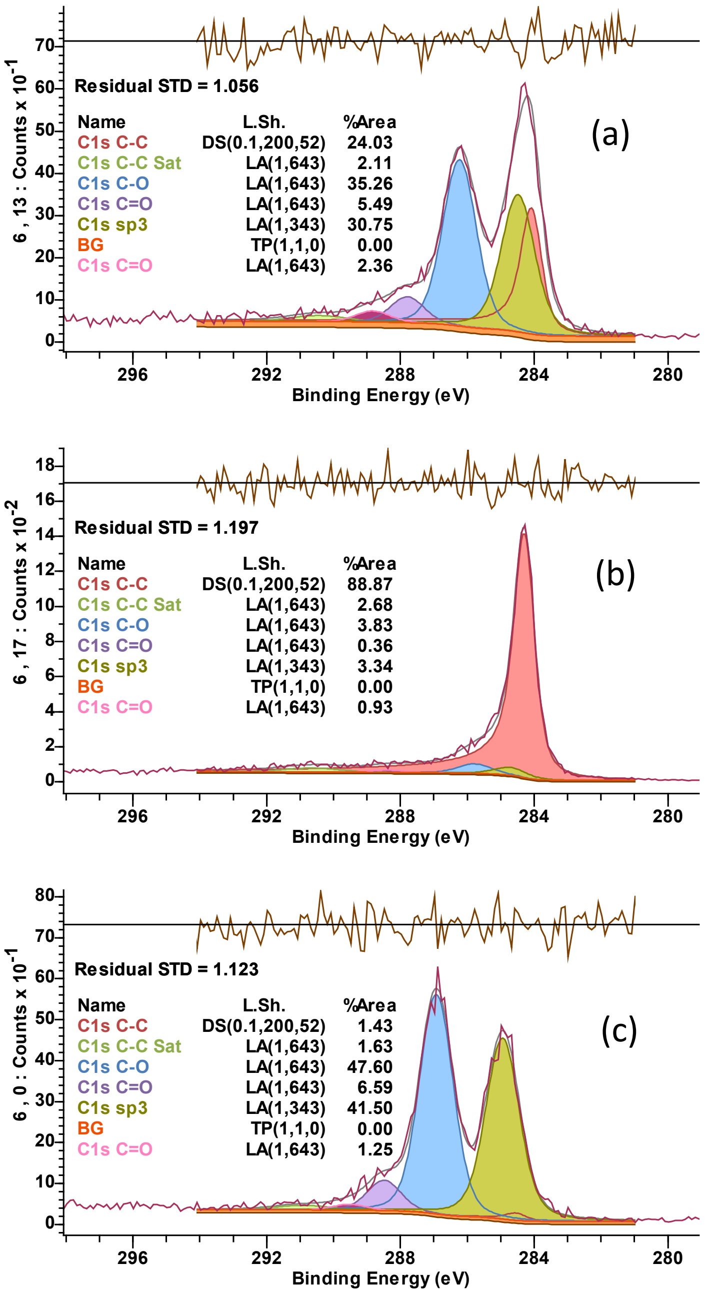

Figure 3. Representative narrow scans from the image in Figure 2 that correspond to (a) a mixture of GO and reduced GO, (b) fully reduced GO, and (c) GO. These peak models all make use of the same components, line shapes, and constraints, as defined in Table 1. The first numbers on the vertical axis label represent pixels (the location of the spectra in the image). TP corresponds to a trapezoidal component that represents background intensity in CasaXPS [30].

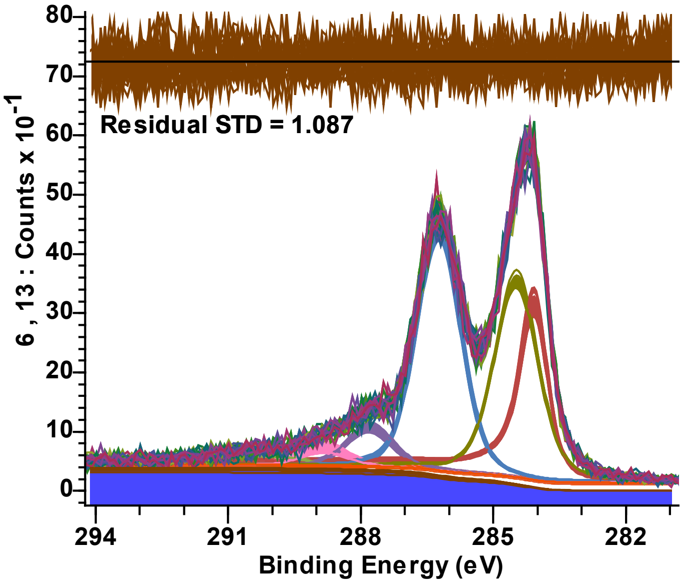

Figure 4. Monte Carlo analysis/test of a peak model illustrating the stability of the model with respect to noise, as applied to the spectrum in Figure 3a.

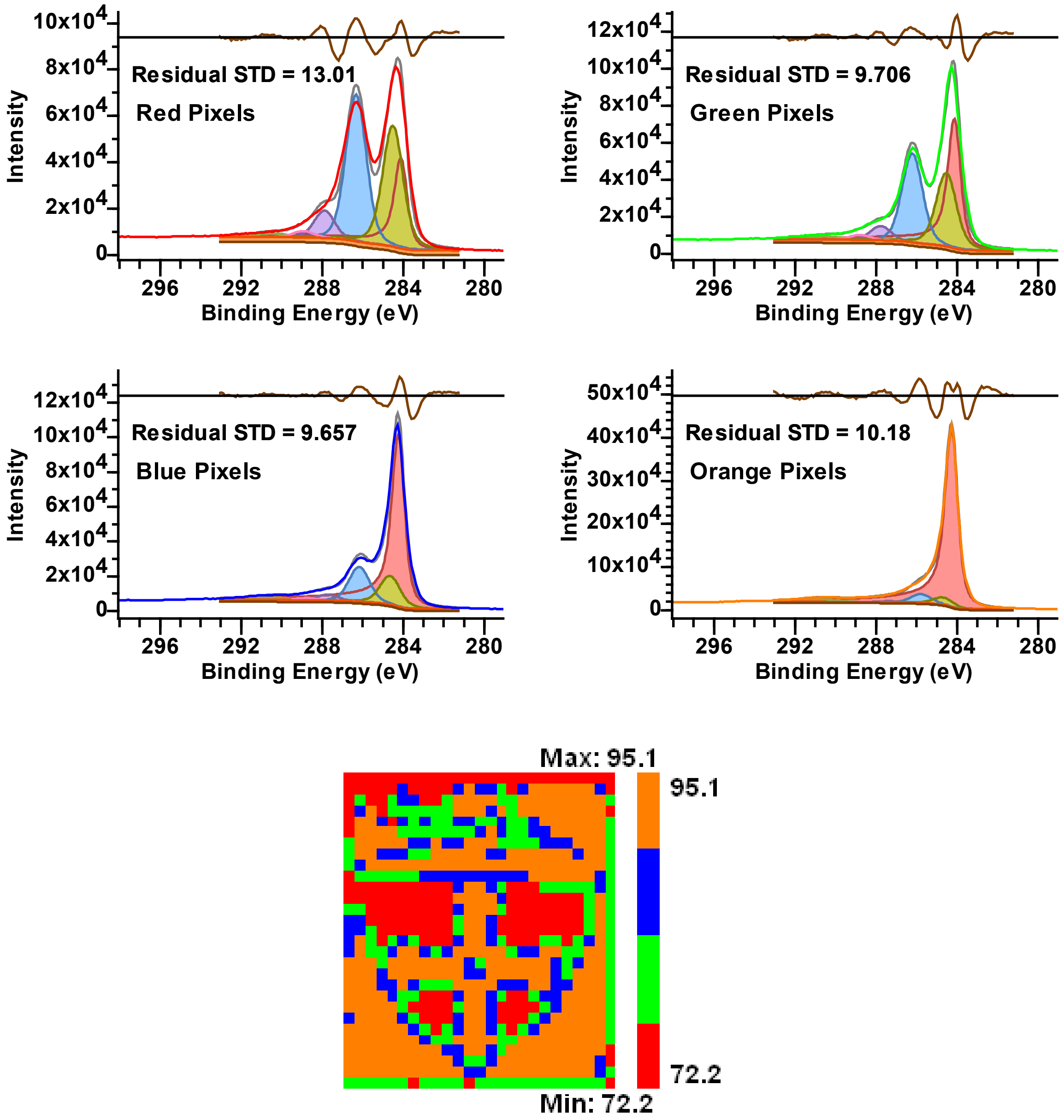

Figure 5. The peak model used in Figure 3 was applied to the data represented in Figure 2. The resulting, colored pixels shown here were obtained/derived from the spatial zones within the image. Red indicates a region in which GO is the dominant material, while orange indicates where rGO is predominantly found. Pixels representing the interface between GO and rGO are marked with green and blue.

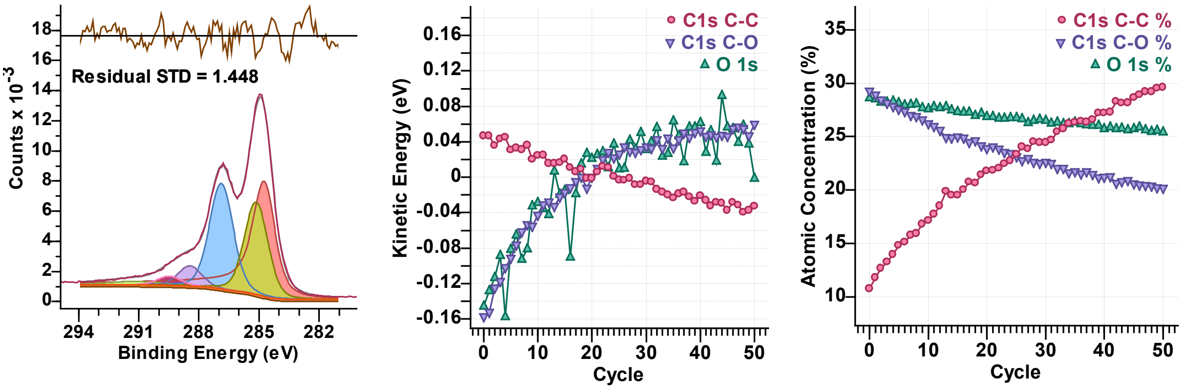

(a) (b) (c)

Figure 6. (a) Spectrum of GO/reduced-GO obtained at a pass energy of 40 and an analysis area of 200 μm that was fitted with the peak model in Figure 3 after relaxing the interval constraints for FWHM in Table 1. (b) Plot of the offset in kinetic energy from the mean component positions for C 1s C-C and C 1s C-O combined with a similar energy offset from the mean calculated for the O 1s signal measured via signal relative to a Shirley background. (c) Relative intensities for the C 1s C-C and C 1s C-O components together with the O 1s intensity converted to atomic concentrations using Scofield cross-sections [35], effective attenuation lengths [36], and the Thermo K-Alpha+ transmission correction.

References

1. Jain, V., Biesinger, M.C., and Linford, M.R. (2018) The Gaussian-Lorentzian Sum, Product, and Convolution (Voigt) functions in the context of peak fitting X-ray photoelectron spectroscopy (XPS) narrow scans. *Appl. Surf. Sci.*, **447**, 548–553.

2. Sherwood, P.M.A. (2019) Rapid evaluation of the Voigt function and its use for interpreting X-ray photoelectron spectroscopic data. *Surf. Interface Anal.*, **51** (2), 254–274.

3. Schmid, M., Steinrück, H.-P., and Gottfried, J.M. (2014) A new asymmetric Pseudo-Voigt function for more efficient fitting of XPS lines. *Surf. Interface Anal.*, **46** (8), 505–511.

4. Spevack, P.A., and McIntyre, N.S. (1993) A Raman and XPS investigation of supported molybdenum oxide thin films. 2. Reactions with hydrogen sulfide. *J. Phys. Chem.*, **97** (42), 11031–11036.

5. Klyushin, A.Y., Rocha, T.C.R., Hävecker, M., Knop-Gericke, A., and Schlögl, R. (2014) A near ambient pressure XPS study of Au oxidation. *Phys. Chem. Chem. Phys.*, **16** (17), 7881.

6. Baltrusaitis, J., Mendoza-Sanchez, B., Fernandez, V., Veenstra, R., Dukstiene, N., Roberts, A., and Fairley, N. (2015) Generalized molybdenum oxide surface chemical state XPS determination via informed amorphous sample model. *Appl. Surf. Sci.*, **326**, 151–161.

7. Nesbitt, H.W., and Banerjee, D. (1998) Interpretation of XPS Mn(2p) spectra of Mn oxyhydroxides and constraints on the mechanism of MnO2 precipitation. *Am. Mineral.*, **83** (3–4), 305 LP – 315.

8. Biesinger, M.C., Lau, L.W.M., Gerson, A.R., and Smart, R.S.C. (2010) Resolving surface chemical states in XPS analysis of first row transition metals, oxides and hydroxides: Sc, Ti, V, Cu and Zn. *Appl. Surf. Sci.*, **257** (3), 887–898.

9. Grosvenor, A.P., Biesinger, M.C., Smart, R.S.C., and McIntyre, N.S. (2006) New interpretations of XPS spectra of nickel metal and oxides. *Surf. Sci.*, **600** (9), 1771–1779.

10. Biesinger, M.C., Payne, B.P., Lau, L.W.M., Gerson, A., and Smart, R.S.C. (2009) X-ray photoelectron spectroscopic chemical state quantification of mixed nickel metal, oxide and hydroxide systems. *Surf. Interface Anal.*, **41** (4), 324–332.

11. Biesinger, M.C., Payne, B.P., Grosvenor, A.P., Lau, L.W.M., Gerson, A.R., and Smart, R.S.C. (2011) Resolving surface chemical states in XPS analysis of first row transition metals, oxides and hydroxides: Cr, Mn, Fe, Co and Ni. *Appl. Surf. Sci.*, **257** (7), 2717–

2730.

12. Grosvenor, A.P., Kobe, B.A., Biesinger, M.C., and McIntyre, N.S. (2004) Investigation of multiplet splitting of Fe 2p XPS spectra and bonding in iron compounds. *Surf. Interface Anal.*, **36** (12), 1564–1574.

13. Baltrusaitis, J., Chen, H., Rubasinghege, G., and Grassian, V.H. (2012) Heterogeneous atmospheric chemistry of lead oxide particles with nitrogen dioxide increases lead solubility: Environmental and health implications. *Environ. Sci. Technol.*, **46** (23).

14. Baltrusaitis, J., Jayaweera, P.M., and Grassian, V.H. (2009) XPS study of nitrogen dioxide adsorption on metal oxide particle surfaces under different environmental conditions. *Phys. Chem. Chem. Phys.*, **11** (37).

15. Hopfengärtner, G., Borgmann, D., Rademacher, I., Wedler, G., Hums, E., and Spitznagel, G.W. (1993) XPS studies of oxidic model catalysts: Internal standards and oxidation numbers. *J. Electron Spectros. Relat. Phenomena*, **63** (2), 91–116.

16. Biesinger, M.C., Brown, C., Mycroft, J.R., Davidson, R.D., and McIntyre, N.S. (2004) X-ray photoelectron spectroscopy studies of chromium compounds. *Surf. Interface Anal.*, **36** (12), 1550–1563.

17. Seah, M.P., and Spencer, S.J. (2003) Ultrathin SiO2 on Si IV. Intensity measurement in XPS and deduced thickness linearity. *Surf. Interface Anal.*, **35** (6), 515–524.

18. Seah, M.P., and White, R. (2002) Ultrathin SiO2 on Si: III mapping the layer thickness efficiently by XPS. *Surf. Interface Anal.*, **33** (12), 960–963.

19. Seah, M.P., and Spencer, S.J. (2002) Ultrathin SiO2 on Si II. Issues in quantification of the oxide thickness. *Surf. Interface Anal.*, **33** (8), 640–652.

20. Seah, M.P., and Spencer, S.J. (2003) Ultrathin SiO2 on Si. I. Quantifying and removing carbonaceous contamination. *J. Vac. Sci. Technol. A Vacuum, Surfaces, Film.*, **21** (2), 345–352.

21. Linford, M.R., Smentkowski, V.S., Grant, J.T., Brundle, C.R., Sherwood, P.M.A., Biesinger, M.C., Terry, J., Artyushkova, K., Herrera-Gómez, A., Tougaard, S., Skinner, W., Pireaux, J.-J., McConville, C.F., Easton, C.D., Gengenbach, T.R., Major, G.H., Dietrich, P., Thissen, A., Engelhard, M., Powell, C.J., Gaskell, K.J., and Baer, D.R. (2020) Proliferation of Faulty Materials Data Analysis in the Literature. *Microsc. Microanal.*, **26** (1), 1–2.

22. Sherwood, P.M.A. (2019) The use and misuse of curve fitting in the analysis of core X-ray photoelectron spectroscopic data. *Surf. Interface Anal.*, **51** (6), 589–610.

23. Major, G.H., Avval, T.G., Moeini, B., Pinto, G., Shah, D., Jain, V., Carver, V., Skinner, W., Gengenbach, T.R., Easton, C.D., Herrera-Gomez, A., Nunney, T.S., Baer, D.R., and Linford, M.R. (2020) Assessment of the frequency and nature of erroneous x-ray photoelectron spectroscopy analyses in the scientific literature. *J. Vac. Sci. Technol. A*, **38** (6), 061204.

24. Baer, D.R., Artyushkova, K., Richard Brundle, C., Castle, J.E., Engelhard, M.H., Gaskell, K.J., Grant, J.T., Haasch, R.T., Linford, M.R., Powell, C.J., Shard, A.G., Sherwood, P.M.A., and Smentkowski, V.S. (2019) Practical guides for x-ray photoelectron spectroscopy: First steps in planning, conducting, and reporting XPS measurements. *J. Vac. Sci. Technol. A*, **37** (3), 031401.

25. Major, G.H., Fairley, N., Sherwood, P.M.A., Linford, M.R., Terry, J., Fernandez, V., and Artyushkova, K. (2020) Practical guide for curve fitting in x-ray photoelectron spectroscopy. *J. Vac. Sci. Technol. A*, **38** (6), 061203.

26. Gengenbach, T.R., Major, G.H., Linford, M.R., and Easton, C.D. (2021) Practical guides for x-ray photoelectron spectroscopy (XPS): Interpreting the carbon 1s spectrum. *J. Vac. Sci. Technol. A*, **39** (1), 013204.

27. Doniach, S., and Sunjic, M. (1970) Many-electron singularity in X-ray photoemission and X-ray line spectra from metals. *J. Phys. C Solid State Phys.*, **3** (2), 285–291.

28. Shirley, D.A. (1972) High-Resolution X-Ray Photoemission Spectrum of the Valence Bands of Gold. *Phys. Rev. B*, **5** (12), 4709–4714.

29. Castle, J.E., and Salvi, A.M. (2001) Interpretation of the Shirley background in x-ray photoelectron spectroscopy analysis. *J. Vac. Sci. Technol. A Vacuum, Surfaces, Film.*, **19** (4), 1170–1175.

30. Fairley, N., Fernandez, V., Richard-Plouet, M., Guillot-Deudon, C., Walton, J., Smith, E., Flahaut, D., Greiner, M., Biesinger, M., Tougaard, S., Morgan, D., and Baltrusaitis, J. (2021) Systematic and collaborative approach to problem solving using X-ray photoelectron spectroscopy. *Appl. Surf. Sci. Adv.*, **5**, 100112.

31. Barlow, A.J., Popescu, S., Artyushkova, K., Scott, O., Sano, N., Hedley, J., and Cumpson, P.J. (2016) Chemically specific identification of carbon in XPS imaging using Multivariate Auger Feature Imaging (MAFI). *Carbon N. Y.*, **107**, 190–197.

32. Gupta, V., Ganegoda, H., Engelhard, M.H., Terry, J., and Linford, M.R. (2014) Assigning Oxidation States to Organic Compounds via Predictions from X-ray Photoelectron Spectroscopy: A Discussion of Approaches and Recommended Improvements. *J. Chem. Educ.*, **91** (2), 232–238.

33. Morgan, D.J. (2021) Comments on the XPS Analysis of Carbon Materials. *C J. Carbon*

Res., **7** (3), 51.

34. Cumpson, P.J., and Seah, M.P. (1992) Random uncertainties in AES and XPS: I: Uncertainties in peak energies, intensities and areas derived from peak synthesis. *Surf. Interface Anal.*, **18** (5), 345–360.

35. Scofield, J.H. (1976) Hartree-Slater subshell photoionization cross-sections at 1254 and 1487 eV. *J. Electron Spectros. Relat. Phenomena*, **8** (2), 129–137.

36. Seah, M.P. (2012) Simple universal curve for the energy-dependent electron attenuation length for all materials. *Surf. Interface Anal.*, **44** (10), 1353–1359.